Heat, Pressure and Light-Induced Interconversion of Bisdithiazolyl Radicals and Dimers

Kristina Lekin,[†] Hoa Phan,[‡] Stephen M. Winter,[†] Joanne W. L. Wong,[†] Alicea A. Leitch,[†] Dominique Laniel,[§] Wenjun Yong,[#] Richard A. Secco,[#] John S. Tse,[⊥] Serge Desgreniers,[§] Paul A. Dube,[∥] Michael Shatruk,*,[‡] and Richard T. Oakley*,[†]

[†]Department of Chemistry, University of Waterloo, Waterloo, Ontario N2L 3G1, Canada

[‡]Department of Chemistry and Biochemistry, Florida State University, Tallahassee, Florida 32306, United States

[§]Department of Physics, University of Ottawa, Ottawa, Ontario K1N 6N5, Canada

[#]Department of Earth Sciences, University of Western Ontario, London, Ontario N6A 5B7, Canada

[⊥]Department of Physics and Engineering Physics, University of Saskatchewan, Saskatoon, Saskatchewan S7N 5E2, Canada

[∥]Brockhouse Institute for Materials Research, McMaster University, Hamilton, Ontario L8S 4M1, Canada

S *Supporting Information*

ABSTRACT: The heterocyclic bisdithiazolyl radical **1b** (R_1 = Me, R_2 = F) crystallizes in two phases. The α-phase, space group $P2_1/n$, contains two radicals in the asymmetric unit, both of which adopt slipped π-stack structures. The β-phase, space group $P2_1/c$, consists of cross-braced π-stacked arrays of dimers in which the radicals are linked laterally by hypervalent 4-center 6-electron S···S−S···S σ-bonds. Variable-temperature magnetic susceptibility measurements on α-**1b** indicate Curie−Weiss behavior (with $\Theta = -14.9$ K), while the dimer phase β-

1b is diamagnetic, showing no indication of thermal dissociation below 400 K. High-pressure crystallographic measurements indicate that the cross-braced π-stacked arrays of dimers undergo a wine-rack compression, but the dimer remains intact up to 8 GPa (at ambient temperature). The resistance of β-**1b** to dissociate under pressure, also observed in its conductivity versus pressure profile, is in marked contrast to the behavior of the related dimer β-**1a** (R_1 = Et, R_2 = F), which readily dissociates into a pair of radicals at 0.8 GPa. The different response of the two dimers to pressure has been rationalized in terms of differences in their linear compressibilities occasioned by changes in the degree of cross-bracing of the π-stacks. Dissociation of both dimers can be effected by irradiation with visible ($\lambda = 650$ nm) light; the transformation has been monitored by optical spectroscopy, magnetic susceptibility measurements, and single crystal X-ray diffraction. The photoinduced radical pairs persist up to temperatures of 150 K (β-**1b**) and 242 K (β-**1a**) before reverting to the dimer state. Variable-temperature optical measurements on β-**1b** and β-**1a** have afforded Arrhenius activation energies of 8.3 and 19.6 kcal mol^{-1}, respectively, for the radical-to-dimer reconversion. DFT and CAS-SCF calculations have been used to probe the ground and excited electronic state structures of the dimer and radical pair. The results support the interpretation that the ground-state interconversion of the dimer and radical forms of β-**1a** and β-**1b** is symmetry forbidden, while the photochemical transformation is symmetry allowed.
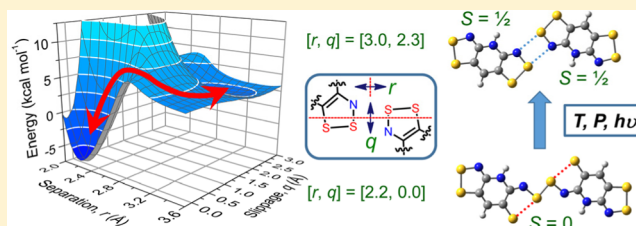
INTRODUCTION

Central to the design of molecule-based electronic and magnetic materials is the understanding of their response to external stimuli.[1] If the molecular and/or crystal structure of a material can be modified by heat, light, or physical pressure, what are the consequences in terms of changes in its electronic or magnetic performance? These issues have played a pivotal role in the development of transition-metal-based spin-crossover compounds, where thermal, pressure, and light-induced spin state switching are all possible.[2] The magnetic properties of organic materials can also be altered by physical stimuli.[3] For example, photoinduced singlet−triplet interconversions in the solid state have been extensively studied, although generally the excited-state lifetimes are short.[4]

For organic radicals and their dimers, the issue of excited-state stability is effectively bypassed, as highly delocalized π-radicals that enjoy remarkable thermal stability are well-known.[5] Many of these systems crystallize as discrete radicals which show interesting charge transport[6] and magnetic properties,[7] while others are strongly associated in the solid state. There is also a "grey zone" where the balance between spin delocalization and covalent bond formation is such that in the solid state the equilibrium between the radical and dimer forms can be easily perturbed. In these cases the thermally driven conversion of the diamagnetic ($S = 0$) dimer into a pair

of paramagnetic ($S = \frac{1}{2}$) radicals can be easily monitored by magnetic susceptibility measurements. In some cases the reverse (cooling) process displays magnetic hysteresis, affording regimes of bistability within which the dimer and (metastable) radical can coexist.[8] The signature of the phase transition may also be detected in conductivity and optical channels, and there is at least one report of photoinduced dimer-to-radical interconversion within the bistable region.[9] Systems in which distinct dimerization modes have been interconverted by light have also been observed.[10] Collectively, these observations have led to interest in the possible use of radical/dimer materials in the development of multifunctional magneto-optical and magneto-electronic information storage devices.[11]

Chart 1

1a, R_1 = Et, R_2 = F
1b, R_1 = Me, R_2 = F
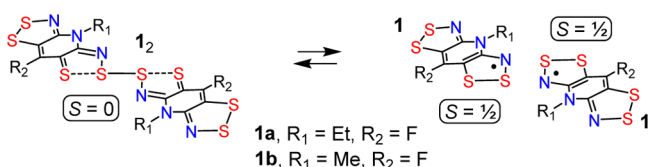
Within this context, we recently reported the preparation and solid-state structural characterization of the heterocyclic bisdithiazolyl radical **1a** (**1**, R_1 = Et, R_2 = F).[12] This compound is dimorphic, the first or α-phase consisting of discrete radicals, while the second or β-phase is based on the closed-shell dimer illustrated in Chart 1. While the formation of a dimer is not, in itself, unusual, the molecular and electronic structures of the dimer most certainly are. The radicals do not associate by a simple coupling of magnetic orbitals, but rather in a manner that requires a configurational $\pi \rightarrow \sigma$ crossover and formation of a hypervalent four-center six-electron (4c-6e) S···S−S···S σ-bond.[13] In the solid state the equilibrium between the dimer and the radical is easily perturbed. The dimer can be opened by heat (at 380 K), by pressure (at ∼0.8 GPa), and by irradiation (λ = 650 nm) at low temperature, with the photogenerated π-radical pair displaying remarkable kinetic stability, surviving to 242 K before reverting to the dimer.[14]

To explore the generality of the solid-state dimer/radical equilibrium observed for β-**1a**, we have prepared the

structurally related radical **1b** (R_1 = Me, R_2 = F). This material is also dimorphic, crystallizing as discrete π-radicals in the α-phase, and as 4c-6e S···S−S···S σ-bonded dimers in the β-phase. Herein we report the structural and magnetic characterization of both phases. As in the case of β-**1a** we have explored the response of β-**1b** to pressure and temperature increases, and also to irradiation with visible (650 nm) light. The results indicate that in spite of the structural similarities between β-**1a** and β-**1b**, the S···S−S···S σ-bond in the dimer of β-**1b** is more robust with respect to variations in P and T, resisting dissociation up to 8 GPa (at ambient temperature) and 400 K (at ambient pressure). However, upon irradiation the dimer unit in β-**1b** is readily cleaved, as in the case of β-**1a**. The interconversion of dimer and radical forms of β-**1b** and the stability and structure of the photogenerated radical state have been probed by optical spectroscopy, magnetic susceptibility measurements, and single crystal X-ray diffraction. Electronic structure calculations, using DFT and CAS-SCF methods, have also been performed on various model structures, with a view to understanding the interconversion pathway between the dimer and radical forms in the ground and excited states. The results support the interpretation that the ground-state interconversion of the dimer and radical forms of β-**1a** and β-**1b** is symmetry forbidden, in the Woodward−Hoffmann sense,[15] while the photochemical transformation[16] is symmetry allowed.

■ RESULTS AND DISCUSSION

Synthesis. Radical **1b** was prepared by reduction of the previously reported triflate salt [**1b**][OTf][17] with decamethyl-ferrocene (DMFc) in degassed MeCN. Crystals of α-**1b** suitable for single crystal X-ray work were obtained by slow codiffusion of carefully degassed solutions of [**1b**][OTf] and DMFc. Fractional sublimation of this material in a three-zone tube furnace at a pressure of 10^{-4} Torr along a temperature gradient of 60−80−120 °C afforded a mixture of α-**1b** (green needles) and β-**1b** (copper blocks) which were manually separated.

Ambient Pressure Crystallography. The crystal and molecular structures of both phases of **1b** have been determined at ambient pressure and temperature by single

Table 1. Crystal Data

	α-**1b**	β-**1b**	β-**1b**	β-**1b**	β-**1b** pre-irradiation	β-**1b** post-irradiation cell I	β-**1b** post-irradiation cell II
formula	$C_6H_3FN_3S_4$	$C_6H_3FN_3S_4$	$C_6H_3FN_3S_4$	$C_6H_3FN_3S_4$	$C_6H_3FN_3S_4$	$C_6H_3FN_3S_4$	$C_6H_3FN_3S_4$
fw	264.35	264.35	264.35	264.35	264.35	264.35	264.35
pressure (GPa)	0	0	2.5	4.9	0	0	0
a, Å	17.301(3)	4.6011(7)	4.1217(2)	3.8654(3)	4.5463(6)	4.789(5)	4.789(5)
b, Å	4.0582(7)	12.732(2)	13.272(1)	13.499(2)	12.780(2)	12.683(14)	12.683(14)
c, Å	26.249(4)	15.912(2)	14.859(1)	14.469(1)	15.735(2)	16.281(16)	16.559(16)
β, deg	92.074(4)	78.949(4)	84.318(5)	86.261(7)	79.741(4)	74.89(3)	71.26(11)
V, Å^3	1841.8(5)	914.8(2)	808.83(5)	753.42(8)	899.6(2)	954.7(17)	954.8(17)
space group	$P2_1/n$	$P2_1/c^a$	$P2_1/c^a$	$P2_1/c^a$	$P2_1/c^a$	$P2_1/c^a$	$P2_1/c^a$
Z	8	4	4	4	4	4	4
temp, K	296(2)	293(2)	293(2)	293(2)	100(2)	100(2)	100(2)
λ, Å	0.71073	0.71073	0.509175	0.509175	0.71073	0.71073	0.71073
solution method	direct methods	direct methods	powder data	powder data	direct methods	direct methods	direct methods
R_p	0.0526	0.0486	0.0105	0.0099	0.0320	0.0838	0.0838
R_{wp}	0.0993	0.0758	0.0158	0.0142	0.0757	0.1932	0.1930

^{a}The unconventional cell setting ($P2_1/c$ with a small value of β) was used so as to allow a direct comparison with related structures (ref 17).

crystal X-ray diffraction. Unit cell and refinement parameters are listed in Table 1, ORTEP drawings of the asymmetric units, with atom numbering schemes, are illustrated in Figure 1, and unit cell drawings of both phases are provided in Figure 2. Selected internal metrics are given in Table 2.
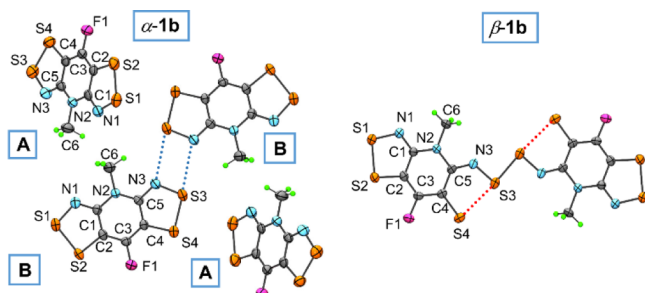

Figure 1. ORTEP drawings (50% thermal ellipsoids) with atom numbering of α-**1b** and β-**1b**. Intermolecular N3···S3′ contacts between centrosymmetric pairs of **B**-radicals in α-**1b** and intramolecular S3···S4 contacts in the dimer β-**1b** are shown with dashed lines.
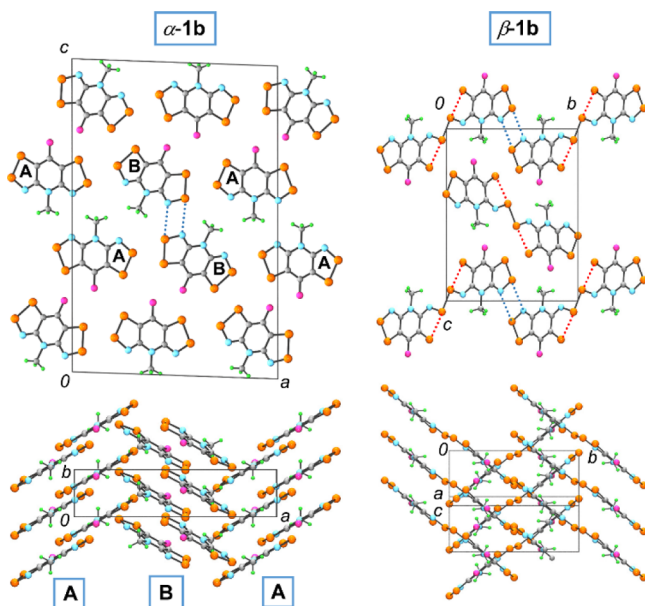

Figure 2. Unit cell drawings of α-**1b** and β-**1b**, viewed parallel to the stacking direction (above) and from the side (below), showing herringbone packing in α-**1b** and cross-bracing in β-**1b**. Intermolecular S···N′ contacts (blue) and intramolecular S···S′ contacts (red) are shown as dashed lines.

Table 2. Selected Metrics for α-1b and β-1b at 0 GPa

	α-**1b** (A)	α-**1b** (B)	β-**1b**
T, K	296(2)	296(2)	293(2)
S1−S2, Å	2.113(2)	2.121(2)	2.090(1)
S3−S4, Å	2.097(2)	2.107(2)	2.797(2)
S1−N1, Å	1.659(4)	1.659(3)	1.650(3)
S3−N3, Å	1.653(4)	1.659(3)	1.643(3)
S2−C2, Å	1.736(4)	1.739(4)	1.713(4)
S4−C4, Å	1.734(4)	1.738(4)	1.670(4)
S3···S3′, Å	–	–	2.169(2)
S3···N3′, Å	–	3.151(3)	–

Crystals of α-**1b** belong to the monoclinic space group $P2_1/n$. With $Z = 8$, there are two distinct molecules (**A** and **B**) in the asymmetric unit (Figure 1), both of which form slipped π-stack arrays running parallel to the b-axis. Figure 2 illustrates the crystal packing in the ac plane, and also the herringbone arrays (viewed down the c-axis) formed by the slipped π-stacks. There are many contacts shorter than the van der Waals separation[18] that lace the structure laterally, but for the sake of later discussion the S3···N3′ (3.151 Å) contacts that link centrosymmetric pairs of **B** radicals are highlighted.

Crystals of β-**1b** belong to the monoclinic space group $P2_1/c$ and consist of interpenetrating, cross-braced slipped π-stacks of σ-dimers, as shown in Figure 2. Each dimer is based on a pair of radicals fused centrosymmetrically to form an approximately linear 4c-6e S4···S3−S3′···S4′ sequence. While the interannular S3−S3′ bond is near that expected for a sulfur−sulfur σ-bond,[19] the S3···S4′ distance (2.797(2) Å) highlighted in red lies at a value intermediate between the sum of the covalent radii (2.1 Å)[20] and the expected van der Waals contact (3.6 Å).[18] At both ends of each dimer are centrosymmetric intermolecular 4-center S_2N_2 contacts (in blue) with d(S1···N1′) = 3.092 Å that link dimers into chain-like arrays. The importance of this superstructure will become apparent later. Within the dimer there is a series of bond length changes relative to those seen in α-**1b**, the most notable being a shortening of the S4−C4 distance, which is consistent with the pseudoquinoidal valence bond formulation shown in Chart 1.
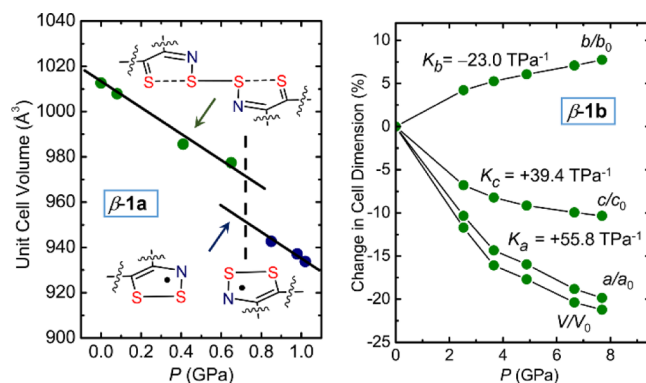

Figure 3. (Left) Unit cell volume of β-**1a** as a function of pressure, with a phase change near 0.8 GPa (from ref 12). (Right) Continuous but highly anisotropic changes in cell dimensions of β-**1b** with increasing pressure, with linear compressibilities $K_{a,b,c}$ (at $P = 0$ GPa) along a, b, and c.

High-Pressure Crystallography. In previous work we showed that the 4c-6e σ-dimer β-**1a** (R_1 = Et) underwent a pressure-induced phase transition near 0.8 GPa (Figure 3), a process which translated, at the molecular level, into a cleavage of the central disulfide linkage and dissociation of the dimer into a pair of π-radicals.[12] To investigate the possibility of a similar behavior for β-**1b** we have explored the response of its structure to applied pressure by powder X-ray diffraction methods, again using synchrotron radiation and diamond anvil cell techniques. Representative powder patterns at 2.5 and 4.9 GPa are available in the Supporting Information (Figure S1). To our surprise we find no evidence of dissociation of β-**1b** with pressurization to 8 GPa nor of a phase change of any other kind. Instead, the changes in cell dimensions over the pressure range 0−8 GPa (Table 1 and Figure 3) reveal a steady but

highly anisotropic compression. The overall volume contraction arises largely from shortening of the a-axis, supported by smaller changes in the c-axis but offset by a pronounced elongation in the b-axis. These differences have been quantified in terms of the isothermal linear compressibility values $K_l = -(\partial l/\partial p)_T$, defined in terms of the fractional changes in length of the a, b, and c axes (Figure 3).[21] This anisotropy, notably the large and relatively rare[22] negative b-axis compressibility, necessarily leads to a collapse of the cross-braced slipped π-stack architecture illustrated in Figure 2, thereby providing a classic demonstration of the "wine-rack" compression mechanism first proposed by Baughman.[23]
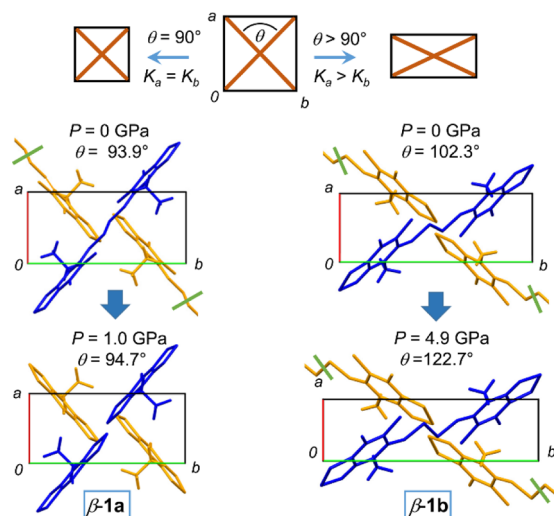

Figure 4. (Top) Linear compressibilities of rectangular beam model subject to hydrostatic pressure, as a function of the dihedral angle θ between the beams (see ref 24). (Below) Changes in cross-bracing angle $\theta = 2 \tan^{-1}(b/2a)$ accompanying isotropic contraction of β-**1a** (left) and wine-rack collapse of β-**1b** (right). In the above drawings the orange molecules are shifted by 0.5 along z relative to the blue molecules.

To explain the markedly different response of these two σ-dimers to pressure, that is, the fact that β-**1a** opens upon compression to just 0.8 GPa, while β-**1b** retains its integrity up to 8 GPa (the limit of the experiment), we have drawn upon the ideas developed by Marmier to rationalize the compressibility of tetragonal beam structures (Figure 4).[24] For such a system, under hydrostatic pressure, linear compressibilities in the horizontal and vertical directions must, by symmetry, be equivalent when the cross-bracing angle between the beams θ is 90°. Under these conditions deformations are directed toward axial compression along the beams; there is no angular torque. However, as θ deviates from 90°, the horizontal and vertical compressibilities will no longer be equal, so that hinging of the beams, and collapse of the wine rack, can occur. This latter situation is precisely what is found in β-**1b**, where the small unit-cell a-vector (4.6011(7) Å at 0 GPa) gives rise to a wide cross-bracing angle $\theta = 2 \tan^{-1}(b/2a) = 102.3°$. A marked anisotropy in the linear compressibilities along the a- and b-axes is therefore to be expected, as is the resulting wine-rack collapse, that is, the contraction of the a-axis, elongation of the b-axis, and increase in the dihedral angle θ (see Figure 4 and Table 1). Essentially, pressure-induced stress in β-**1b** is relieved by rotation of the dimers, without disturbing the 4c-6e σ-bonded unit.

In β-**1a**, the a-axis is longer (5.3256(3) Å at 0 GPa), and the cross-braced π-stacks are more steeply inclined, affording a value of the dihedral angle $\theta = 93.9°$. Because the phase change from dimer to radical takes place at relatively low pressure, we do not have sufficient data below the phase change to estimate linear compressibilities with any accuracy. However, given the proximity of θ to 90° it is likely that K_a and K_b are similar, in which case the pressure should be focused axially along the dimers (the molecular beams). Comparison of the structure of β-**1a** at 0 GPa and at 1.0 GPa (Figure 4) is consistent with this prediction. Both the a- and b-axes contract slightly, as a result of which the dihedral angle θ barely changes, suggesting a relatively isotropic 2D compression directed along the long axis of the dimers. The origin of the phase change, involving the rupture of the dimer, is therefore a direct consequence to the response of the dimer to axially resolved stress. Consequent cleavage of the interannular disulfide linkage generates two independent radicals which are then free to slide past one another, thereby absorbing the compression. This effect is evident in the contraction in the overall length of the dimer (the molecular beam) that accompanies its dissociation.
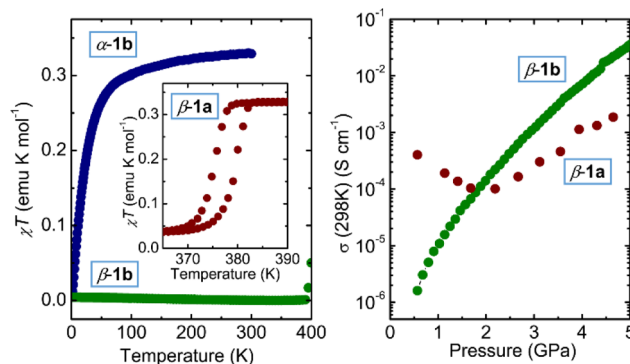

Figure 5. Plots of χT versus T for α-**1b**, β-**1b** (left) and β-**1a** (left, inset) and plots of σ(298 K) versus pressure for β-**1a** and β-**1b** (right). Data for β-**1a** from ref 12.

Magnetic Susceptibility and Conductivity Measurements. Magnetic susceptibility (χ) measurements have been performed on both the α- and β-phases of **1b** using a SQUID magnetometer operating at a field (H) of 0.1 T. Figure 5 shows data collected over the range $T = 2-300$ K for α-**1b** and $T = 2-400$ K for β-**1b**, presented as plots of χT against T. In the range $50-300$ K the α-phase displays Curie–Weiss behavior, and a linear fit affords values of $C = 0.346$ emu K mol^{-1} and $\Theta = -14.9$ K. Given the fact that there are two independent spin centers in the unit cell, no attempt was made to fit the data to a more specific magnetic model. The data for the β-phase displays the classic signature of a diamagnetic material. There is a very small paramagnetic "tail" apparent in χ vs T plots below 20 K, from which we estimate a radical defect concentration near 1%. The material remains diamagnetic up to 400 K, the limit of the experiment, although the final high-temperature data points suggest the onset of opening of the dimers just above 400 K. In the case of β-**1a**, complete thermal conversion of the dimer to the radical was observed at 380 K (Figure 5).[12]

The absence of pressure-induced phase change noted in the high pressure crystallographic data on β-**1b** are supported by high pressure conductivity measurements, performed using a cubic anvil press. In previous work on β-**1a** we had noted an inflection in the conductivity of β-**1a** between 0 and 2 GPa

(Figure 5), an effect that was interpreted in terms of the electronic changes associated with the rollover of the semiconducting hypervalent σ-dimer to a Mott-insulating radical-based material.[12] By contrast, we find that the conductivity σ(298 K) of β-**1b** does not decrease upon pressurization but rather increases steadily from 10^{-6} S cm^{-1} at 0 GPa to near 10^{-2} S cm^{-1} at 5 GPa, as expected for a continuous, pressure-driven band gap closure.
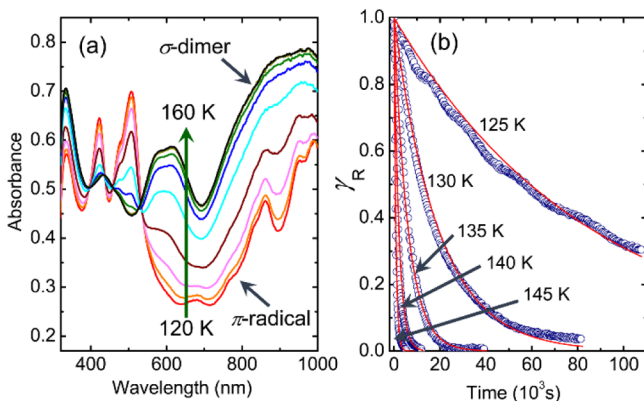

Figure 6. (a) Evolution of the optical absorption spectrum obtained after irradiation of a microcrystalline film of β-**1b** with a 650 nm laser at 100 K, and subsequent warming to 160 K. The spectra shown after the one at 120 K (red line) were recorded with a 5 K step at a heating rate of 0.2 K min^{-1}. (b) Mole fraction γ_R of the photogenerated radical form of β-**1b** as a function of time at different temperatures. The solid red lines indicate the fit to single-exponential decay kinetics.

Optical Measurements. In earlier work we demonstrated the photoinduced dimer-to-radical dissociation of β-**1a** and introduced the concept of light-induced radical trapping (LIRT).[14] The resulting paramagnetic π-radical form remained kinetically stable to 220 K, above which temperature it began a thermally activated relaxation to the diamagnetic σ-dimer, with $T_\downarrow$ = 242 K. In the present work we have examined the possibility of LIRT for β-**1b**. To this end a microcrystalline film of β-**1b** was embedded in epoxy resin and irradiated with a white-light source ($\sim$10 mW cm^{-2}) for 2 min at 100 K. Optical absorption spectra were recorded in transmission mode both before and after irradiation (Figures 6a and S2). As in the case of β-**1a**, the broad absorption of the dimer in the 600–800 nm range was substantially reduced as a result of irradiation, and new bands at 420 and 510 nm appeared. To minimize the absorption of the photogenerated radical, we subsequently used a 650 nm laser for variable temperature optical, magnetic and crystallographic measurements. The microcrystalline film of β-**1b** embedded in epoxy resin was irradiated at $\sim$15 mW cm^{-2} for 30 s at 60 K, and the resulting optical absorption spectrum was monitored as a function of increasing temperature. The spectrum of the photogenerated radical (red curve in Figure 6a) remained essentially unchanged at 120 K, but at 125 K and above the broad absorption signature of the dimer in the 600–800 nm range gradually reappeared and the radical-based bands at 420 and 510 nm vanished. Spectra recorded at and above 150 K matched the original spectrum of the dimer.

Relaxation of the LIRT state was examined by monitoring the isothermal decay of the 510 nm band at different temperatures (Figure 6b). At 125 K, only 40 % of the radical form was converted to the dimer after 11 h. At higher temperatures, the relaxation rate constant increases, as expected

for a thermally activated process. At 145 K, the relaxation was complete after about 1.4 h. The relaxation kinetics in the thermally activated region was satisfactorily described by a single-exponential decay model (Figure S3). The fit of the relaxation rate constants to the Arrhenius equation (Figure 6b) afforded a relaxation barrier E_{act} = 8.3(2) kcal mol^{-1}, somewhat smaller than that found for β-**1a** (19.6 kcal mol^{-1}). This finding is consistent with the difference in the radical-to-dimer relaxation temperatures, 150 K for β-**1b** and 242 K for β-**1a**. Possible origins for this difference are discussed below.
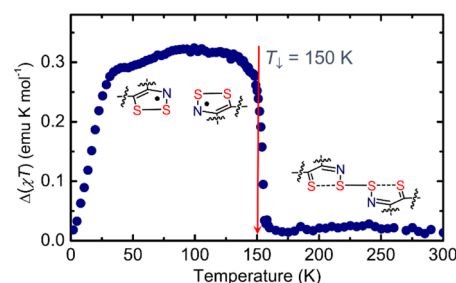

Figure 7. Change in $\Delta(\chi T)$ (at H = 0.1 T) observed for a microcrystalline film of β-**1b** after irradiation with λ = 650 nm at 10 K and warming at a rate of 3 K min^{-1} from 2 to 100 K, 0.2 K min^{-1} from 100 to 170 K, and 3 K min^{-1} from 170 to 300 K.

Photomagnetic Measurements. A microcrystalline film of β-**1b** was placed on a flexible Kapton tape and mounted on the tip of a quartz rod connected to an optical fiber. The sample was lowered into a SQUID magnetometer, cooled to 10 K, and irradiated with the 650 nm laser, which resulted in a gradual increase of the measurable magnetic response (Figure S3), in accord with the generation of the LIRT state. After 2 h, the irradiation was stopped, the sample was cooled down to 2 K, and the magnetic susceptibility was measured in a warming mode under an applied field of H = 0.1 T. Figure 7 shows the difference plot for the χT product of the sample before and after irradiation. At low temperatures, $\Delta(\chi T)$ is suppressed by antiferromagnetic exchange coupling between radicals, as observed in the α-**1b** polymorph and the LIRT state of β-**1a**. With increasing temperature, $\Delta(\chi T)$ quickly rises, reaching a plateau value of 0.28–0.31 emu K mol^{-1} between 40 and 145 K, in agreement with the nearly quantitative photoconversion of the diamagnetic (S = 0) σ-dimer to a pair of paramagnetic (S = $^1/_2$) radicals. The $\Delta(\chi T)$ value drops abruptly above 145 K and becomes close to zero at 155 K. These results are consistent with the thermally activated relaxation to the σ-dimer state, as was also observed by optical absorption spectroscopy. The $\Delta(\chi T)$ product of the LIRT state does not reach the value of 0.375 emu K mol^{-1} expected for a pure S = $^1/_2$ system (with g = 2). This may be the result of incomplete photoconversion due to defect trapping and/or to measurement errors caused by the small amount of sample used (0.48(1) mg) to ensure penetration of the radiation into the sample and allow complete conversion.

Crystal Structure of the LIRT State. To investigate more closely the structural changes associated with photoinduced dissociation of β-**1b** we collected X-ray diffraction data on a single crystal of β-**1b** cooled to 90 K and irradiated with a 650 nm laser for 4 h. Analysis of the diffraction data collected subsequently at 100 K confirmed a quantitative σ-dimer to π-radical pair transformation within the common space group $P2_1/c$; difference electron-density maps did not reveal any

significant peaks that would suggest the presence of a residual fraction of the dimer. While the quality of the resulting refinement (Table 1) is good, the process of data collection was hampered by the tendency of the crystals to fracture upon irradiation. As a result, many crystals (with decreasing size) had to be examined, until one was found that survived the photoinduced structural changes without splintering. This problem was not encountered during related measurements on β-**1a**,[14] a behavioral difference that will be discussed below.
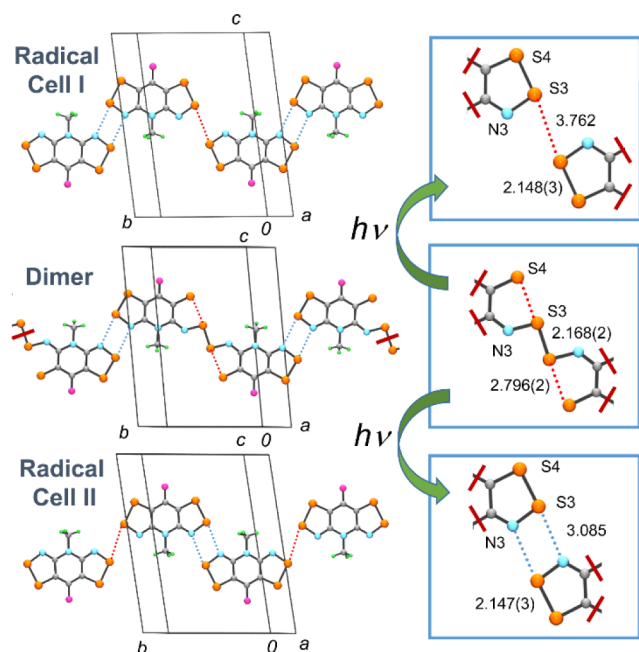

Figure 8. Chains of dimers in β-**1b** (at 100 K), with the hypervalent disulfide bond located at the $x = y = z = \frac{1}{2}$ inversion center. Also shown are two solutions for the photogenerated radical (at 100 K) based on different cell settings. In cell **I** the long S···S′ contacts are set at the $x = y = z = \frac{1}{2}$ inversion center, and in cell **II** the 4-center S_2N_2 contacts are located at this point.

Interpretation of the details of structural changes accompanying the photodissociation provided an unexpected challenge. The problem became apparent upon close inspection of the crystal packing, in particular the position of the dimer and photoinduced radicals with respect to the inversion centers in the unit cell (Figure 8). Prior to irradiation, the σ-dimer straddles the inversion center at $x = y = z = \frac{1}{2}$, and each end is linked laterally to neighboring dimers by close 4-center S_2N_2 interactions with $d(S1\cdots N1') = 3.044$ Å located at inversion centers on the cell faces; this produces a chain-like array of dimers. In the postirradiation structure, the liberated radicals remain linked laterally, with radicals locked by 4-center S_2N_2 interactions at one end and long intermolecular S···S′ contacts at the other. Both types of links straddle inversion centers, as in the parent dimer structure. The question that arises, however, is the genealogy of the links in the radical-based structure, and the inversion centers associated with them. How do these inversion centers relate to those found in the dimer? The dilemma is illustrated in Figure 8, which provides two cell setting options (**I** and **II**) for the radical-based structures at 100 K, each based on different but equivalent cell settings. In cell **I** the long S···S′ contacts are set at the $x = y = z = \frac{1}{2}$ inversion center, while in cell **II** the 4-center S_2N_2 contacts are located at this point.

While both cells represent acceptable structural solutions, evolution to each one from a common dimer implies a different dimer-to-radical conversion pathway. The use of cell **I** requires dissociation of the dimer along a track which keeps the hypervalent S4···S3−S3′···S4′ sequence approximately collinear, while cell **II** requires that the separation of the dimer be associated with slippage of the radical pair to form a 4-center S_2N_2 arrangement. The question as to which is the more likely path (**I** or **II**) followed upon dissociation of the dimer is discussed below.

The crystallographic conundrum encountered for β-**1b** was not an issue in β-**1a**, even though the packing is very similar, with centrosymmetric dimers arranged into chains. In the latter structure, however, there is a unique alignment of ethyl groups with respect to the cross-braced π-stacks, and there is only one cell setting for the resulting dimer that preserves this orientation. As a result transformation of the dimer to a structure that closely resembles that illustrated for cell **II** could be specified without ambiguity. Outside of the issue regarding the interconversion pathway(s) between the dimer and radical forms there are other differences in the behavior of β-**1b** and β-**1a**. For example, the unit cell of β-**1b** experiences a significant (5.8%) increase in volume during the dimer-to-radical transformation, a result consistent with the failure of pressure to produce the radical pair state of β-**1b**, as this would necessarily require a contraction in the unit cell. By contrast, the small (2.1%) contraction in the cell volume following photodissociation of β-**1a** is consistent with easy access to this state under pressure, as observed. The significant expansion in the cell volume of β-**1b** upon photodissociation may also account for the tendency of the crystals to fragment during the phase transition (the "jumping crystal" phenomenon).[8a,25]

Theoretical Calculations. To place the experimental results in context, it is useful to review briefly the range of dimerization modes known for heterocyclic thiazyl and selenazyl π-radicals. The radicals are often bound cofacially, through one[26] or more[27,28] sites, usually involving heavy (S/Se) atoms, although for Se-containing dimers some more unusual modes have been observed.[29] The tendency to form multicenter bonds is also found in purely organic π-radicals, and in recent years this has given rise to the moniker "pancake" π-bonding.[30] While there is continued debate over the nature and strength of the weak interactions in these nominally π-dimers,[31] it is convenient to describe the covalent contribution to the binding energy in terms of the coupling of two π-SOMOs on neighboring radicals, as illustrated in Figure 9 for the cofacial association of a simple 1,2,3-dithiazolyl.[32]

Formation of the π-dimer involves no change in electronic configuration as the two radicals approach and, as a result, there is no activation barrier to the association (in the absence of lattice effects). By contrast, the lateral association of two dithiazolyl π-radicals to form a 4c-6e S···S−S···S σ-bond, that is, along a path that keeps all four sulfur atoms collinear, will involve an activation energy E_{act} (Figure 9), even at the molecular level, as the process is symmetry forbidden. In molecular orbital terms, the origin of the activation energy stems from the fact that there is a $(\pi)^1(\pi)^1 \leftrightarrow (\sigma)^2$ configurational reorganization accompanying the interconversion.

To generate a more quantitative description of the energy changes accompanying the thermally driven dimer-to-radical interconversion, we carried out a series of density functional theory (DFT) calculations at the (U)B3LYP/6-31G(d,p) level
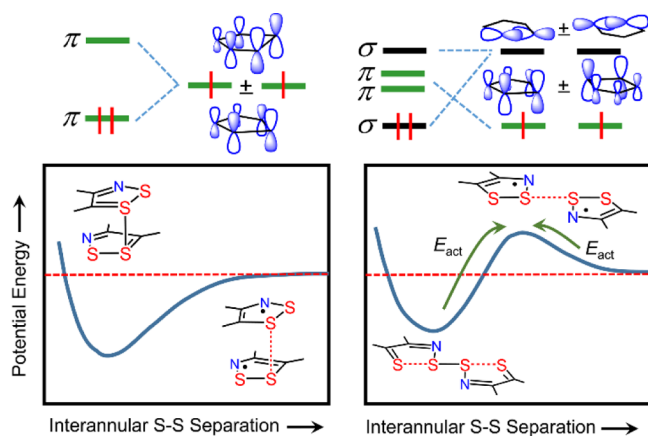
Figure 9. Qualitative potential energy profiles for the cofacial association of two dithiazolyl radicals into π-dimer (left) and the lateral association of two dithiazolyls into a 4c-6e S···S—S···S σ-dimer (right). The latter process, which involves a $(\pi)^1(\pi)^1 \leftrightarrow (\sigma)^2$ configurational crossover, is symmetry forbidden, and subject to a thermal activation energy E_{act} in both directions.
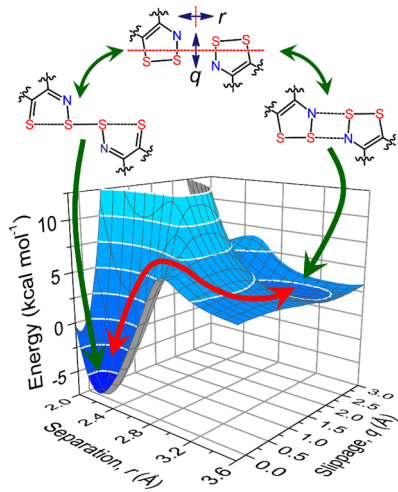

Figure 10. Plate separation (r) and slippage (q) parameters (in Å) used to map the dimer-to-radical transformation of a (C_{2h} optimized) bisdithiazolyl radical **1** ($R_1 = R_2 = H$), and (U)B3LYP/6-31G(d,p) electronic energy surface for the lowest singlet state (closed shell or broken symmetry) for the dimer-to-radical transformation. Specific geometries are designated as $[r, q]$ points.

on a prototypal dimer **1**, with $R_1 = R_2 = H$, tracking the electronic energy of the lowest energy singlet state as a function of (i) the separation of the two radicals r, and (ii) the degree of slippage q, both defined in Figure 10. Systematic variation of these two parameters allows an approximate mapping of the ground-state energy surface for the dimer-to-radical interconversion. Outside of the two constraints imposed on r and q, full geometry optimization within the confines of C_{2h} symmetry was invoked. The resulting electronic energy surface, representing the lower of the closed shell singlet σ-dimer state and the broken symmetry singlet of the π-radical pair, is illustrated in Figure 10.

While these calculations ignore the critical solid-state effects provided by the surrounding lattice, which prevent the π-radical pair from drifting apart, they nonetheless provide qualitative insight into the potential energy surface that is traversed as the dimer-to-radical conversion proceeds. For example, moving

outward by stretching the central S—S bond from $[r, q]$ = [2.0, 0.0] to [3.6, 0.0] reveals the energy profile anticipated on symmetry arguments (Figures 9 and S6), with a global minimum near [2.2, 0.0], as found experimentally in β-**1a** and β-**1b**, and an estimated barrier to dimer dissociation near 13 kcal mol^{-1}. The barrier for the reverse process, the recombination of the radicals, is near 3 kcal mol^{-1}. Also noteworthy is the shallow metastable minimum for the π-radical pair near [3.0, 2.3] which lies some 2 kcal mol^{-1} below the [3.6, 0.0] point. This extra stabilization occasioned by mutual slippage of the radicals (large q) is reminiscent of the weak intermolecular 4-center S_2N_2 binding commonly found in thiadiazoles and related compounds.[33] The broad funnel-like maximum which separates the minima for the starting dimer and final radical pair also suggests that their direct thermal dissociation by simultaneous contraction (or elongation) of r and q is energetically less favorable than one along a more circuitous route involving sequential changes in r and q (highlighted by the red arrow in Figure 10). The high-temperature (and high pressure) structural data on β-**1a** are consistent with a mechanism based on separation followed by slippage of the liberated radical pair, to afford the metastable minimum suggested by the DFT calculations. We cannot comment on β-**1b**, as we have no high-temperature structural data, and it does not dissociate under pressure up to 8 GPa.

While experimental information on the high-temperature dimer-to-radical conversion is limited to β-**1a**, the availability of low temperature structural data on both the dimer and radical forms of both β-**1a** and β-**1b** presents the opportunity for consideration of the pathway for the thermally driven recombination of the two photogenerated radicals to their respective dimers. In the case of the radical state of β-**1b**, there is the problem (noted above) arising from the choice of cell settings (**I** and **II** in Figure 8), each of which implies a different reaction pathway. While we cannot make a definitive choice between these two mechanisms, we believe that use of cell **I** allows a better explanation for the lower $T_\downarrow$ and E_{act} value observed for β-**1b** relative to β-**1a**.

To make this case we refer to Figure 11, which compares structural data for the photoinduced radicals and dimers of β-**1a** and β-**1b**, as collected at 100 K. For β-**1a** the radical-to-dimer conversion can be described in terms of back-slippage of the
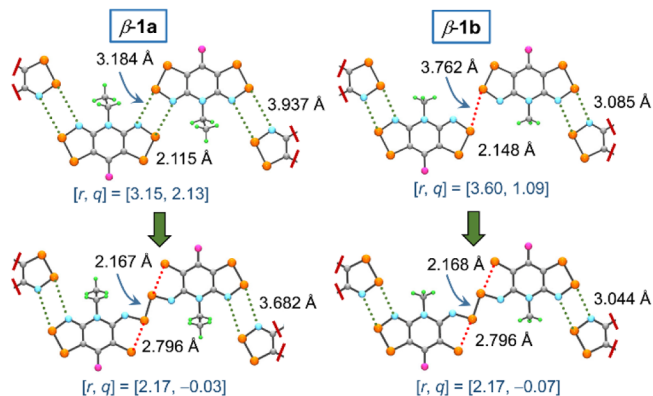

Figure 11. Comparison of thermally driven radical-to-dimer recombination for β-**1a** (left) and β-**1b** (right), based on structural data obtained at 100 K. The $[r, q]$ coordinates are defined in Figure 10. The pathway for β-**1b** assumes cell setting **I** (see Figure 8) for the radical.

radicals (a decrease in q), followed by contraction along r, that is to say, S−S bond formation. Note that geometries of the two end-points suggest that throughout the process the radical pair and subsequent dimer remain relatively isolated laterally from their neighbors along the chain. The terminal intermolecular 4-center S_2N_2 contacts shorten from 3.937 Å in the radical to 3.682 Å in the dimer, but in neither case can these interactions be considered energetically significant. Such is not the case in β-**1b**. If we select cell setting **I**, as shown in Figure 11, the terminal 4-center S_2N_2 contacts in the radical are already short (3.085 Å), and in the course of the dimerization they experience a small contraction (to 3.044 Å). Essentially the outer ends or "tails" of the radical pair remain pinned at a single inversion center throughout the transformation. That being the case, dimerization reduces simply to closure of the central unit or "head" of the radical pair, the $[r, q]$ coordinates [3.6, 1.1] of which are consistent with a stretched disulfide with relatively little slippage. Inspection of the DFT potential energy surface indicates this geometry lies in a high-energy region of the potential surface. Its reversion to the dimer involves little more than contraction along r, a process associated with a smaller energy barrier than that required from the more slipped 4-center, metastable minimum position. This observation may explain the lower E_{act} found for β-**1b**. The alternative pathway, based on cell setting **II** (Figure 8), requires a greater overall structural change. The previously pinned 4-center S_2N_2 units must slip backward and contract into a hypervalent σ-dimer, while the radical pair ends slide forward and close into 4-center S_2N_2 units. The net result is a switch in location of the molecular "heads" and "tails" between inversion centers. While we cannot discount this pathway, we feel it is more likely to be associated with a higher activation energy.

LIRT Mechanism. Having discussed the possible pathways for radical-to-dimer recombination and demonstrated that thermal dissociation/reassociation along the ground-state energy surface is inhibited by an energy barrier arising from symmetry forbidden $(\pi)^1(\pi)^1 \leftrightarrow (\sigma)^2$ configurational crossover, we now address the mechanism for photodissociation of the dimers. To explore this issue we have examined their low-lying excited states using a combination of TD-DFT and CAS-SCF methods. As a first step we performed a TD-DFT calculation on the gas phase dimer of **1b**, using a C_{2h} optimized geometry at the B3LYP/6-31G(d,p) level, which revealed four strongly allowed singlet $\pi-\pi$ excitations above 400 nm, all to states of B_u symmetry. Calculated wavelengths and oscillator strengths are provided in Figure 12, along with a spectral simulation; experimental solid-state spectra for both β-**1a** and β-**1b** are also shown. Despite the appealing correspondence between the number and positions of the calculated (gas phase) and experimental (crystalline film) peaks, we are reluctant to attempt definitive assignments, since in the solid-state intermolecular electronic perturbations (Davydov splitting)[34] are likely to be strong. However, the TD-DFT results support the view that all the accessible excited states in the visible region are generated by transitions between occupied and virtual π-orbitals (Table S5 and Figure S7). They do not alter σ/π occupancy, and as a result, dimer dissociation through any of these B_u states is symmetry forbidden. In the absence of the involvement of other states, Franck−Condon excitation to any one of these states, followed by nonradiative relaxation,[35] should eventually regenerate the dimer in its ground state.

Photoinduced separation of these dimers must therefore involve a state accessed indirectly, and to explore this possibility
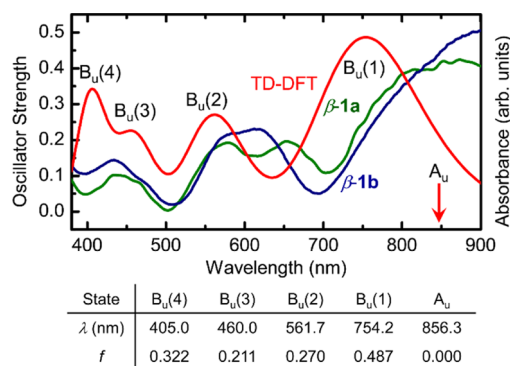

Figure 12. Thin film electronic spectra of β-**1a** (green) and β-**1b** (blue), with B3LYP/6-31G(d,p) TD-DFT calculated states and simulated spectrum (red) for a C_{2h} optimized (gas phase) dimer of **1b**. Calculated wavelengths (nm) and oscillator strengths (f) are shown below.

State	$B_u(4)$	$B_u(3)$	$B_u(2)$	$B_u(1)$	A_u
λ (nm)	405.0	460.0	561.7	754.2	856.3
f	0.322	0.211	0.270	0.487	0.000

we considered the role of the lowest-lying excited state, which is of A_u symmetry, highlighted in Figure 12. While this state cannot be generated by direct photoexcitation ($f = 0.000$), it should be readily accessible from the B_u states, since the lower symmetry afforded by the crystal lattice (C_i) renders them equivalent. As a result nonradiative relaxation to the A_u state from any of the B_u states should be fast. The orbital changes accompanying the formation of this A_u state may be understood with reference to Figure 13, which illustrates its formation via electron excitation from the S−S σ-bonding a_g HOMO-1 to the S−S π-bonding a_u LUMO, which is a net $\sigma \rightarrow \pi$ process. By contrast, and as noted earlier, the $B_u(1)$ state is generated by $\pi \rightarrow \pi$ excitation from the S−S π-antibonding b_u HOMO to the S−S π-bonding a_u LUMO. We assert that in the B_u state dimer dissociation is symmetry forbidden, but in the A_u state it is symmetry allowed.
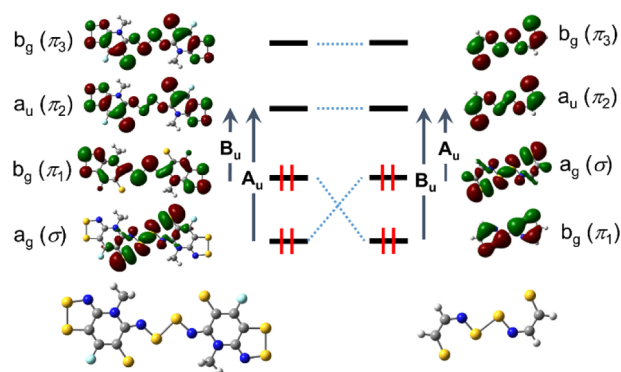

Figure 13. Correlation diagram tracking the B3LYP/6-31G(d,p) frontier orbitals of a gas phase σ-dimer **1b** and a model monocyclic dithiazolyl σ-dimer (right), with transitions to low-lying excited A_u and B_u states probed by TD-DFT methods and/or CAS-SCF (4,4) methods.

To support this conclusion, we would have liked to use CAS-SCF methods to track the energies of all excited states, the four photoaccessible B_u states and the indirectly accessible A_u state, as a function of the separation and slippage coordinates r and q introduced earlier, with a view to exploring the resulting energy surfaces and their suitability for providing a pathway for photochemical dissociation. Given, however, the size of the full dimer and the resulting chemically active space required to

explore the full manifold of excited states, we focused our attention on a smaller model dimer built from two prototypal dithiazolyls, as shown in Figure 13. The CAS-SCF (4,4) energies for the A_g $[(\pi_1)^2(\sigma)^2]$ ground state, and the A_u $[(\pi_1)^2(\sigma)^1(\pi_2)^1]$ and B_u $[(\pi_1)^1(\sigma)^2(\pi_2)^1]$ excited states of this system were calculated using B3LYP/6-31G(d,p) starting orbitals. For each state the geometry was separately optimized over a range of $[r, q]$ points, to afford the triple-decker energy surface diagram shown in Figure 14. Because of its smaller π-system, this model cannot provide any information on the higher lying B_u states of the full dimer. It does, however, within the confines of a CAS (4,4) space, preserve the orbital character of the A_u and first B_u states of the full dimer. Moreover, given that all four excited B_u states in the full dimer are based on $(\pi)^2 \rightarrow (\pi)^1(\pi)^1$ excitations, the behavior of the potential surface of the lowest B_u state with respect to variations in r and q is probably representative of the others.
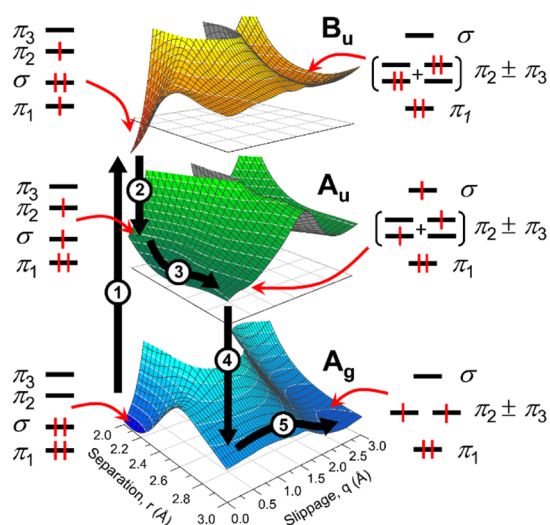

Figure 14. CAS-SCF (4,4) energy surfaces for the singlet ground state A_g and two lowest excited singlet states A_u and B_u of a model dithiazolyl dimer or radical pair, plotted as a function of the separation (r) and slippage (q) parameters defined in Figure 10. Black arrows highlight the suggested (see text) pathway for light-induced conversion of the dimer to a pair of radicals. Configuration drawings are referenced to the orbitals shown in Figure 13. White contour lines are drawn at 0.15 eV intervals; the energy curves have arbitrary relative offset.

As expected, the CAS-SCF energy surface for the ground state is qualitatively similar to that predicted by DFT methods applied to the full dimer (Figure 10). There is a deep minimum near $[r, q] = [2.2, 0.0]$, a shallow minimum near [3.0, 2.5], and an energy maximum near [2.6, 0.0], which provides the barrier for the thermal reconversion of the radical pair to the dimer. The B_u excited state is even more strongly bound, as expected given that the excitation is $\pi^* \rightarrow \pi$ (Figure 13). As a result, whether this state is accessed photochemically, as implied by the black arrow (step 1), or by relaxation from a higher lying B_u state, separation of the dimer remains blocked by a large energy barrier, a result anticipated on the basis of orbital symmetry. In the absence of a pathway for dissociation, nonradiative relaxation (step 2) allows access to the low-lying A_u state. As in the full dimer, this state can be described in terms of depopulation of the a_g orbital, which is σ-bonding across the inner S−S linkage and σ-antibonding across the outer S···S

partners of the 4-center S···S−S···S sequence.[12,13] As a result the outer S−S distances are shortened (to 2.45 Å), heralding the evolution of the dimer toward discrete, open-shell radicals. In step 3 the two dithiazolyl rings separate, as the A_u state is not bound along the r-direction. In essence, stretching and rupture of the central S−S bond is not symmetry forbidden. While there is a large barrier to motion in the q-coordinate, thermal energy may allow some vibrational movement in this direction. Eventually, nonradiative relaxation from the A_u state to the ground state A_g surface (step 4) then affords two radicals that are sufficiently separated (large r) to resist thermal recombination to the dimer. The energy surface traversed along step 5, also probed at the DFT level on the full scale model (Figure 10), is associated with a relatively low barrier to slippage along the q-direction. Depending on solid-state effects, the final geometry may lie at the large q end of this trajectory, as in β-**1a**, or retain a relatively small value of q, as implied by the use of cell **I** for β-**1b**.[36]

SUMMARY AND CONCLUSIONS

We have provided the results of a comprehensive examination of the response of the β-phase of the bisdithiazolyl σ-dimer **1b** to heat, pressure, and light and compared its performance under these stimuli with that of the related dimer β-**1a**. Variable-temperature magnetic measurements on both compounds indicate the thermal barrier to dissociation of β-**1b** is slightly greater than in β-**1a**. However, the fact that both β-**1a** and β-**1b** sublime into radicals near 120 °C (in vacuo) implies that their thermal dissociation enthalpies are comparable. The differences in their behavior under pressure are more dramatic; while β-**1a** dissociates with relatively mild loading (~0.8 GPa), the dimer structure of β-**1b** is retained until at least 8 GPa. This dichotomy can be related to the cross-braced architecture generated by the intersecting π-stacks. In β-**1a** the π-stacks intersect with a nearly orthogonal angle, so that isotropic compression is focused along the dimer unit, causing its rupture into a radical pair. In β-**1b** intersection of the π-stacks is not orthogonal, and isotropic compression leads to a wine-rack collapse[23] of the cross-braced structure, without disturbing the integrity of the dimer. In light of the ease of pressure-induced opening of β-**1a**, it is appealing to consider whether these hypervalent σ-dimers might find application in the design of materials with specific pressure-dependent magnetic properties. While it is well-known that the spin state of spin-crossover compounds can be altered by pressure,[37] the high-pressure form (with large crystal field splitting) is usually low spin, so that an increase in pressure switches OFF (or down) the magnetic signal. By contrast, the magnetic properties of β-**1a** are switched ON (from the $S = 0$ to the $S = \frac{1}{2}$ state) under pressure, a change which may offer a much greater sensitivity to molecule-based pressure sensors.

The results of DFT calculations on model systems related to β-**1a** and β-**1b** reinforce the idea that, even in the gas phase, the dimer-to-radical interconversion experiences an energy barrier since it is symmetry forbidden,[15] requiring a $(\sigma)^2$ to $(\pi)^1(\pi)^1$ configurational crossover. We have, however, successfully demonstrated that dissociation of both β-**1a** and β-**1b** in the solid state can be readily effected photochemically. TD-DFT calculations have been used to identify the low-lying excited states of the dimer that are accessible directly or indirectly by irradiation, and the results of CAS-SCF calculations are consistent with dissociation being mediated by a low-lying $(\sigma)^1(\pi)^1$ A_u excited state. This phenomenon, which we denote

light-induced radical trapping or LIRT, leads to a magnetic signature, a spin state change from $S = 0$ to $S = {}^1/_2$, akin to that produced by the LIESST effect observed in transition-metal-based spin crossover (SCO) compounds.[2d,38] Both processes are associated with a configurational reorganization, implying an inherent activation barrier at the molecular level. In the case of the LIRT effect, the structural changes for the radical-to-dimer recombination are larger than those encountered during a high-spin to low-spin reversion in a transition-metal ion. The somewhat higher thermal stability of the LIRT state of these radical σ-dimers relative to the LIESST state of SCO complexes is therefore both predictable and encouraging.[39] We believe these findings will be of value in the development of new radical-based materials displaying a magneto-optical response.

■ EXPERIMENTAL SECTION

General Methods and Procedures. Reagent grade acetonitrile (MeCN) was dried by distillation from P_2O_5 and CaH_2. Decamethylferrocene (DMFc) was obtained commercially, and [**1b**][OTf] was prepared as previously described.[17] Fractional sublimations of **1b** were performed in an ATS series 3210 three-zone tube furnace, mounted horizontally, and linked to a series 1400 temperature control system. Infrared spectra (Nujol mulls, KBr optics) were recorded on a Nicolet Avatar FTIR spectrometer at 2 cm^{-1} resolution. Elemental analyses were performed by MHW Laboratories, Phoenix, AZ.

Preparation of 8-Fluoro-4-methyl-4H-bis[1,2,3]dithiazolo-[4,5-b:5,4-e]pyridin-3-yl, 1b. All glassware was soaked overnight in dilute HNO_3, washed with deionized water followed by distilled water, and finally dried at 100 °C overnight. Magnetic stir bars were glass-covered. A sample of [**1b**][OTf] (700 mg, 1.69 mmol) and DMFc (585 mg, 1.79 mmol) was combined in 20 mL of degassed (four freeze–pump–thaw cycles) MeCN at 0 °C. After the mixture was stirred for 4 h at room temperature, the black-green microcrystalline product (α-**1b**) was filtered off and washed with 5 × 10 mL of MeCN. Yield, 405 mg (1.51 mmol, 84%). IR: 1510 (s), 1462 (s), 1352 (s), 1280 (s), 1238 (s) 1161 (m), 1125 (m), 1059 (w), 1026 (s), 937 (w), 867 (m), 791 (s), 760 (w), 713 (m), 678 (s), 653 (w), 637 (s), 577 (w), 559 (w), 516 (m), 500 (w), 472 (s). Radical phase α-**1b**: Thin green needles of α-**1b** suitable for crystallographic work were obtained by slow codiffusion of degassed (four freeze–pump–thaw cycles) solutions of [**1b**][OTf] (28 mg, 0.0677 mmol) in 10 mL MeCN and DMFc (23 mg, 0.0705 mmol) in 15 mL MeCN. Dimer phase β-**1b**: Crystals suitable for crystallographic work, as well as transport property measurements, were obtained by vacuum sublimation of the bulk material at 10^{-4} Torr along a temperature gradient of 120–80–60 °C. This gave afforded bronze blocks of β-**1b**, along with some green needles of α-**1b**, which were separated manually. IR: 1538 (s), 1508 (m), 1443 (s), 1396 (w), 1212 (w), 1100 (m), 1045 (m), 869 (w), 840 (m), 772 (s), 709 (w), 661 (s), 616 (w), 561 (w), 517 (w), 473 (m). Anal. calcd for β-**1b**, $C_6H_3FN_3S_4$: C, 27.26; H, 1.14; N, 15.89. Found: C, 26.96; H, 1.61; N, 15.61.

Single Crystal Crystallography. Single crystals of both phases (α- and β-) of **1b** were glued to glass fibers with epoxy. X-ray data were collected using ω scans with a Bruker APEX I CCD detector on a D8 three-circle goniometer and Mo Kα (λ = 0.71073 Å) radiation. The data were scanned using Bruker's SMART program and integrated using Bruker's SAINT software.[40] The structures were solved by direct methods using SHELXS-90[41] and refined by least-squares methods on F^2 using SHELXL-97,[42] as incorporated in the SHELXTL suite of programs.[43] For photodissociation studies, a small crystal (0.01 × 0.01 × 0.14 mm^3) of β-**1b** was embedded in epoxy resin and mounted on a cryoloop (Hampton Research). The resin was allowed to age for 24 h before the cryoloop was placed on a goniometer head of a Bruker D8 Quest diffractometer equipped with a microfocus Mo Kα X-ray source. The crystal was centered at room temperature, to avoid photoinduced dissociation that was observed to occur at lower temperatures under irradiation from the alignment

lamp. After the crystal alignment was complete, the lamp was turned off and the crystal was cooled down in N_2 cold stream to 100 at 5 K min^{-1} in the dark. The X-ray diffraction data on the σ-dimer form were collected as ω-scans at 0.35° step width. To obtain the X-ray diffraction data on the LIRT state, the crystal was cooled down to 90 at 5 K min^{-1} and irradiated by a 650 nm continuous diode laser (~15 mW cm^{-2}) prior to the data collection. The crystal was rotated by 90° after each hour of irradiation to allow for uniform and quantitative conversion of the dimer to the radical form. After 4 h, the laser was turned off, the crystal temperature was adjusted to 100 K, and X-ray diffraction data were recorded as ω-scans at 0.35° step width. The data processing, crystal structure solution, and refinement followed the route described above. Difference electron-density maps did not reveal any significant peaks (max = +0.93, min = −0.67 e Å^{-3}) that might suggest the presence of a residual fraction of dimer.

High-Pressure Powder Crystallography. High-pressure X-ray diffraction data on β-**1b** were collected on the High Energy X-ray Materials Analysis (HXMA) beamline of the Canadian Light Source, using synchrotron radiation (λ = 0.509175 Å) and a powdered sample mounted in a diamond anvil cell with low viscosity (1 cst) polydimethylsiloxane as the pressure-transmitting medium. The diffraction data were collected at room temperature as a function of increasing pressure; details of the experiment are given elsewhere.[44] A total of five data sets over the pressure range 0−7.7 GPa were indexed using DICVOL,[45] and two of these (2.5 and 4.9 GPa) were solved starting from a model based on the ambient pressure crystal structure of β-**1b**. During the initial refinement, performed using DASH,[46] a rigid-body constraint was maintained, but the sulfur positions were later released to optimize within the plane of the molecule. Final Rietveld[47] refinement, using fixed atomic positions and isotropic thermal parameters with an assigned value of 0.025, was performed in GSAS.[48] Atomic positions obtained from DASH were not further refined in GSAS, as a result of which standard deviations for atomic coordinates are not reported. Final unit cell parameters and refinement parameters indices R_p and R_{wp} are listed in Table 1. Linear compressibilities $K_l = -(\partial l / \partial p)_T$ ($l = a, b, c$) were obtained by fitting a plot of ln l/l_0 versus p (the ambient temperature data) to a polynomial function $Ap + Bp^2 + Cp^3 + ...$, then setting the value of K_l (at $p = 0$) = A.[22c]

Conductivity Measurements. High pressure−temperature conductivity experiments on α-**1b** were carried out with 1000 ton cubic anvil press[49] using pyrophyllite $(Al_4Si_8O_{20}(OH)_4)$ as the pressure transmitting medium. Sample pressure was determined from previous calibrations[50] of the applied hydraulic load against pressures of structure transformations in standards at room temperature (Bi I−II at 2.54 GPa, Tl I−III at 3.70 GPa, and Ba at 5.5 GPa). The pressure cell included Pt disk electrodes in contact with the precompacted powder samples contained in a boron nitride $(\sigma_{BN} = 10^{-11}$ S cm^{-1}) cup. Four-wire ac (Solartron 1260 Impedance Analyzer) resistance measurements were made at a frequency of 1 kHz. The contiguous disk-shaped sample was extracted from the recovered pressure cell, and the sample geometry was measured to convert resistance to conductivity.

Magnetic Measurements. Initial dc magnetic susceptibility measurements on both phases of **1b** were performed over the temperature range 2−400 K on a Quantum Design MPMS SQUID magnetometer operating at H = 0.100 T. Diamagnetic corrections were made using Pascal's constants.[51] For the photomagnetic measurements on β-**1b** a Quantum Design MPMS-XL SQUID magnetometer was employed. The sample was irradiated in the SQUID chamber by using a commercial Fiber Optic Sample Holder (FOSH, Quantum Design). The sample of β-**1b** was finely ground and dispersed on a funnel-like sample holder made of Kapton tape, which was placed against the end of a fused silica rod connected to an optical fiber. The fiber was coupled to a continuous diode laser operating at the wavelength of 650 nm and power of ~20 mW cm^{-1}. In a typical experiment, the magnetic susceptibility (χ) was first measured as the sample was cooled down in the dark from 300 to 10 K under applied magnetic field of 0.100 T. After the temperature was stabilized at 10 K, the light source was turned on, resulting in the increase of the observed magnetization value. The irradiation was performed for

about 2 h, and then the laser was turned off, and the sample cooled down to 2 K. The temperature dependence of magnetic susceptibility was measured in the heating mode at 0.1 T. The warming rate was 3 K min^{-1} from 2 to 100 K, 0.2 K min^{-1} from 100 to 170 K, and 3 K min^{-1} from 170 to 300 K.

Optical Measurements. Optical absorption spectra on β-**1b** were recorded in the transmission mode in the 300−1000 nm range using a Cary 50 Bio UV−vis spectrometer. The temperature was controlled by a closed cycle cryostat with the coldfinger from Advanced Research Systems, Inc., coupled with an APD, HC-2 He compressor and a Digital Temperature Controller capable of operating at 4−400 K. A polycrystalline sample was finely ground and embedded in epoxy, which was attached to a copper plate with a 0.5 mm aperture placed at the end of the coldfinger. After the sample was cooled at 5 K min^{-1}, it was irradiated with different light sources. In the experiments with white light, a commercial source (∼10 mW cm^{-2}) was used, and the sample was irradiated for ∼2 min at 100 K. In the other experiments, a 650 nm continuous diode laser (∼15 mW cm^{-2}) was used, and the sample was irradiated for ∼30 s at 60 K. After irradiation, the sample was warmed up from 60 to 100 at 3 K min^{-1} and then from 100 to 160 at 0.2 K min^{-1}, and the absorption spectra were collected at specific temperatures shown in Figure 6a.

For kinetic measurements the sample of β-**1b** was cooled to 100 K and irradiated with the 650 nm laser (∼15 mW cm^{-2}) for 30 s. The temperature was then increased to the desired temperature (125−145 K, Figure 6b). Data collection started after a 1 min delay to equilibrate the temperature. The relaxation from dimer to radical pair was monitored as a function of time through the evolution of single-wavelength absorption at 510 nm.

Electronic Structure Calculations. All DFT calculations were performed with the Gaussian 09W suite of programs,[52] using the (U)B3LYP hybrid functional and a polarized, split-valence basis set with double-ζ (6-31G(d,p)) functions. Ground-state geometries and energies were calculated for several models, including **1** with $R_1 = R_2 =$ H, and a smaller version based on two monocyclic dithiazolyl rings. Full geometry optimization for the dimers was invoked within the constraints of C_{2h} symmetry, and TD-DFT methods were used to compute the energies and oscillator strengths of the excited states of these geometries. The resulting simulation for the dimer of **1b** (Figure 12) is plotted using a Gaussian line shape and a 0.33 eV line width. A TD-DFT calculation was also performed on a model radical **1** ($R_1 = R_2$ = H), and a comparison of its computed spectrum with the experimental spectra of the photogenerated radicals **1a** and **1b** at 100 K is provided in Figure S8. DFT energy surface calculations for both the closed shell and broken symmetry singlet states (Figure S6) were performed on models constrained within C_{2h} and adjusted by the parameters $r = 2.0–4.0$ Å and $q = −0.2–3.0$ Å to give a grid of ∼225 points. The resulting two-dimensional $[r, q]$ dependent surface displayed in Figure 10 represents the lower in energy of these two states. Similar two-dimensional CAS-SCF energy surfaces for the monocyclic dithiazolyl ring model were calculated with the ORCA package[53] using a 6-31G(d,p) basis set and a complete (4,4) active space that included those orbitals shown in Figure 13. For each chosen $r = 2.0–3.0$ Å and $q = 0.0–3.0$ Å, starting orbitals for the CAS-SCF calculation were obtained from an initial single point B3LYP calculation. Separate CAS-SCF calculations were then performed on each of the lowest A_g, A_u, and B_u roots, with the geometry of each excited state separately optimized within C_s symmetry while constraining r and q. Several starting geometries were investigated to ensure converged final geometries.

ASSOCIATED CONTENT

Supporting Information

Details of crystallographic data collection and structure refinement for α-**1b** and β-**1b**, tables of atomic coordinates, bond distances and angles, and isotropic thermal parameters in CIF format. High-pressure powder diffraction patterns, details of kinetic analysis and magnetic measurements, DFT surface energy and TD-DFT calculations, with sample G09 archival files. This material is available free of charge via the Internet at http://pubs.acs.org.

AUTHOR INFORMATION

Corresponding Authors
oakley@uwaterloo.ca
shatruk@chem.fsu.edu

Notes
The authors declare no competing financial interest.

REFERENCES

(1) (a) *Molecular Switches*, 2nd ed.; Feringa, B., Ed.; Wiley-VCH: Weinheim, Germany, 2001. (b) *Photoinduced Phase Transitions*; Nasu, K., Ed.; World Scientific Publishing: Singapore, 2004. (c) Létard, J.-F.; Guionneau, P.; Goux-Capes, L. *Top. Curr. Chem.* **2004**, *235*, 221. (d) Bousseksou, A.; Molnár, G.; Salmon, L.; Nicolazzi, W. *Chem. Soc. Rev.* **2011**, *40*, 3313.

(2) (a) Decurtins, S.; Gütlich, P.; Köhler, C. P.; Spiering, H.; Hauser, A. *Chem. Phys. Lett.* **1984**, *105*, 1. (b) Decurtins, S.; Gütlich, P.; Hasselbach, K. M.; Hauser, A.; Spiering, H. *Inorg. Chem.* **1985**, *24*, 2174. (c) Sato, O.; Iyoda, T.; Fujishima, A.; Hashimoto, K. *Science* **1996**, *272*, 704. (d) Hauser, A. *Top. Curr. Chem.* **2004**, *234*, 155. (e) Sato, O.; Tao, J.; Zhang, Y.-Z. *Angew. Chem., Int. Ed.* **2007**, *46*, 2152. (f) *Spin Crossover in Transition Metal Compounds I−III*; Gütlich, P., Goodwin, H. A., Eds.; Springer: Berlin, Heidelberg, Germany, 2004. (g) *Spin Crossover Materials: Properties and Applications*; Halcrow, M. A., Ed.; J. Wiley & Sons: Chichester, U.K., 2013. (h) Guionneau, P. *Dalton Trans.* **2014**, *43*, 382.

(3) (a) Ratera, I.; Veciana, J. *Chem. Soc. Rev.* **2012**, *41*, 303. (b) Nakatsuji, S. *Chem. Soc. Rev.* **2004**, *33*, 348.

(4) (a) Zhu, Z.; Bally, T.; Stracener, L. L.; McMahon, R. J. *Am. Chem. Soc.* **1999**, *121*, 2863. (b) Sajimon, M. C.; Ramaiah, D.; Suresh, C. H.; Adam, W.; Lewis, F. D.; George, M. V. *J. Am. Chem. Soc.* **2007**, *129*, 9439. (c) Günaydın-Sen, Ö.; Fosso-Tande, J.; Chen, P.; White, J. L.; Allen, T. L.; Cherian, J.; Tokumoto, T.; Lahti, P. M.; McGill, S.; Harrison, R. J.; Musfeldt, J. S. *J. Chem. Phys.* **2011**, *135*, 241101. (d) Modarelli, D. A.; Lahti, P. M. *J. Am. Chem. Soc.* **1991**, *113*, 6329.

(5) (e) *Stable Radicals: Fundamentals and Applied Aspects of Odd-Electron Compounds*; Hicks, R. G., Ed.; J. Wiley & Sons: Chichester, U.K., 2010.

(6) (a) Cordes, A. W.; Haddon, R. C.; Oakley, R. T. *Adv. Mater.* **1994**, *6*, 798. (b) Oakley, R. T. *Can. J. Chem.* **1993**, *71*, 1775. (b) Cordes, A. W.; Haddon, R. C.; Oakley, R. T. *Phosphorus, Sulfur, Silicon Relat. Elem.* **2004**, *179*, 673. (e) Morita, Y.; Suzuki, S.; Sato, K.; Takui, T. *Nat. Chem.* **2011**, *3*, 197. Haddon, R. C. *ChemPhysChem* **2012**, *13*, 3581.

(7) (a) Rawson, J. M.; Alberola, A.; Whalley, A. *J. Mater. Chem.* **2006**, *16*, 2560. (b) Awaga, K.; Tanaka, T.; Shirai, T.; Umezono, Y.; Fujita, W. *C. R. Chim.* **2007**, *10*, 52. (c) Hicks, R. G. *Org. Biomol. Chem.* **2007**, *5*, 1321. (d) Preuss, K. E. *Dalton Trans.* **2007**, 2357. (e) Lahti, P. *Adv. Phys. Org. Chem.* **2011**, *45*, 93. (f) Boeré, R. T.; Roemmele, T. L. *Comp. Inorg. Chem. II* **2013**, *1*, 375. (g) Rawson, J. M.; Hayward, J. J. *Handbook of Chalcogen Chemistry: New Perspectives in Sulfur, Selenium*

and Tellurium; Devillanova, F. , Du Mont, W.-W., Eds.; Royal Society of Chemistry: Cambridge, U.K., 2013; Vol 2; pp 69−98.

(8) (a) Barclay, T. M.; Cordes, A. W.; George, N. A.; Haddon, R. C.; Itkis, M. E.; Mashuta, M. S.; Oakley, R. T.; Patenaude, G. W.; Reed, R. W.; Richardson, J. F.; Zhang, H. *J. Am. Chem. Soc.* **1998**, *120*, 352. (b) Fujita, W.; Awaga, K. *Science* **1999**, *286*, 261. (c) McManus, G. D.; Rawson, J. M.; Feeder, N.; van Duijn, J.; McCinnes, E. J. L.; Novoa, J. J.; Burriel, R.; Palacio, F.; Oliete, P. *J. Mater. Chem.* **2001**, *11*, 1992. (d) Itkis, M. E.; Chi, X.; Cordes, A. W.; Haddon, R. C. *Science* **2002**, *296*, 1443. (e) Brusso, J. L.; Clements, O. P.; Haddon, R. C.; Itkis, M. E.; Leitch, A. A.; Oakley, R. T.; Reed, R. W.; Richardson, J. F. *J. Am. Chem. Soc.* **2004**, *126*, 14692. (f) Pal, S. K.; Bag, P.; Sarkar, A.; Chi, X.; Itkis, M. E.; Tham, F. S.; Donnadieu, B.; Haddon, R. C. *J. Am. Chem. Soc.* **2010**, *132*, 17258.

(9) Matsuzaki, H.; Fujita, W.; Awaga, K.; Okamoto, H. *Phys. Rev. Lett.* **2003**, *91*, 017403.

(10) Edkins, R. M.; Probert, M. R.; Robertson, C. M.; Howard, J. A. K.; Beeby, A. *RSC Adv.* **2014**, *4*, 5351.

(11) (a) Miller, J. S. *Angew. Chem., Int. Ed.* **2003**, *42*, 27. (b) Hicks, R. G. *Nat. Chem.* **2011**, *3*, 189. (c) Rawson, J. M.; Hayward, J. J. In *Spin-Crossover Materials: Properties and Applications*; Halcrow, M. A., Ed.; J. Wiley & Sons: Chichester, U.K., 2013; p 235.

(12) Lekin, K.; Winter, S. M.; Downie, L. E.; Bao, X.; Tse, J. S.; Desgreniers, S.; Secco, R. A.; Dube, P. A.; Oakley, R. T. *J. Am. Chem. Soc.* **2010**, *132*, 16212.

(13) Hypervalent 4c-6e bonds involving combinations of S, Se, and/ or Te are well-known for systems in which the terminal chalcogens are saturated. See, for example: (a) Nakanishi, W.; Hayashi, S.; Toyota, S. *Chem. Commun.* **1996**, 371. (b) Nakanishi, W.; Hayashi, S.; Arai, T. *Chem. Commun.* **2002**, 2416. (c) Nakanishi, W.; Hayashi, S.; Morinaka, S.; Sasamori, T.; Tokitoh, N. *New J. Chem.* **2008**, *32*, 1881. (d) Sharma, S.; Selvakumar, K.; Singh, V. P.; Zade, S. S.; Singh, H. B. *Phosphorus, Sulfur Silicon Relat. Elem.* **2008**, *183*, 827.

(14) Phan, H.; Lekin, K.; Winter, S. M.; Oakley, R. T.; Shatruk, M. *J. Am. Chem. Soc.* **2013**, *135*, 15674.

(15) (a) Woodward, R. B.; Hoffmann, R. *Angew. Chem., Int. Ed.* **1969**, *8*, 781. (b) Woodward, R. B.; Hoffmann, R. *The Conservation of Orbital Symmetry*; Verlag Chemie: Weinheim, Germany, 1970.

(16) There are few examples of photochemically driven inter-conversions involving thiazyl radicals. For example, see Brooks, W. V. F.; Burford, N.; Passmore, J.; Schriver, M. J.; Sutcliffe, L. H. *J. Chem. Soc., Chem. Commun.* **1987**, 69.

(17) Leitch, A. A.; Yu, X.; Robertson, C. M.; Secco, R. A.; Tse, J. S.; Oakley, R. T. *Inorg. Chem.* **2009**, *48*, 9874.

(18) (a) Bondi, A. *J. Phys. Chem.* **1964**, *68*, 441. (b) Dance, I. *New J. Chem.* **2003**, *27*, 22. (c) Eramian, H.; Tian, Y.-H.; Fox, Z.; Beneberu, H. Z.; Kertesz, M. *J. Phys. Chem. A* **2013**, *117*, 14184.

(19) (a) Knop, O.; Boyd, R. J.; Choi, S. J. *J. Am. Chem. Soc.* **1988**, *110*, 7299. (b) Denk, M. *J. Eur. J. Inorg. Chem.* **2009**, 1358.

(20) Chen, C. M.; Dojahn, J. G.; Wentworth, W. E. *J. Phys. Chem. A* **1997**, *101*, 3088.

(21) The pressure dependence of the unit cell parameters β-**1b** finds a parallel in the behavior of its isostructural selenium-based analog, although the overall compressibility of the latter is smaller, as intermolecular interactions are stronger. See: Lekin, K.; Leitch, A. A.; Tse, J. S.; Bao, X.; Secco, R. A.; Desgreniers, S.; Ohishi, Y.; Oakley, R. T. *Cryst. Growth Des.* **2012**, *12*, 4676.

(22) (a) Cairns, A. B.; Catafesta, J.; Levelut, C.; Rouquette, J.; van der Lee, A.; Peters, L.; Thompson, A. L.; Dmitriev, V.; Haines, J.; Goodwin, A. L. *Nat. Mater.* **2013**, *12*, 212. (b) Cairns, A. B.; Thompson, A. L.; Tucker, M. G.; Haines, J.; Goodwin, A. L. *J. Am. Chem. Soc.* **2012**, *134*, 4454. (c) Goodwin, A. L.; Keen, D. A.; Tucker, M. G. *Proc. Natl. Acad. Sci. U.S.A.* **2008**, *105*, 18708. (d) Li, W.; Probert, M. R.; Kosa, M.; Bennett, T. D.; Thirumurugan, A.; Burwood, R. P.; Parinello, R. P.; Howard, J. A. K.; Cheetham, A. K. *J. Am. Chem. Soc.* **2012**, *134*, 11940. (e) Haines, J.; Chateau, C.; Léger, J. M.; Bogicevic, C.; Hull, S.; Klug, D. D.; Tse, J. S. *Phys. Rev. Lett.* **2003**, *91*, 015503. (f) Zhou, M.; Wang, K.; Men, Z.; Sun, C.; Li, Z.; Liu, B.; Zou, G.; Zou, B. *CrystEngComm* **2014**, *16*, 4084.

(23) (a) Baughman, R. H.; Galvao, D. S. *Nature* **1993**, *365*, 735. (b) Baughman, R. H.; Shacklette, J. M.; Zakhidov, A. A.; Stafstrom, S. *Nature* **1998**, *392*, 362. (c) Baughman, R. H.; Stafstrom, S.; Cui, C. X.; Dantas, S. O. *Science* **1998**, *279*, 1522.

(24) Barnes, D. L.; Miller, W.; Evans, K. E.; Marmier, A. *Mech. Mater.* **2012**, *46*, 123.

(25) (a) Zamir, S.; Bernstein, J.; Greenwood, D. J. *Mol. Cryst. Liq. Cryst.* **1994**, *242*, 193. (b) Dunitz, J. D.; Bernstein, J. *Acc. Chem. Res.* **1995**, *28*, 193. (c) Naumov, P.; Sahoo, S. C.; Zakharov, B. A.; Boldyreva, E. V. *Angew. Chem., Int. Ed.* **2013**, *52*, 9990.

(26) (a) Hayes, P. J.; Oakley, R. T.; Cordes, A. W.; Pennington, W. T. *J. Am. Chem. Soc.* **1985**, *107*, 1346. (b) Oakley, R. T.; Reed, R. W.; Cordes, A. W.; Craig, S. L.; Graham, S. B. *J. Am. Chem. Soc.* **1987**, *109*, 7745. (c) Boeré, R. T.; Roemmele, T. L.; Yu, X. *Inorg. Chem.* **2011**, *50*, 5123.

(27) (a) Britten, J. F.; Clements, O. P.; Cordes, A. W.; Haddon, R. C.; Oakley, R. T.; Richardson, J. F. *Inorg. Chem.* **2001**, *40*, 6820. (b) Beer, L.; Cordes, A. W.; Myles, D. J. T.; Oakley, R. T.; Taylor, N. J. *CrystEngChem.* **2000**, *2*, 109. (c) Parvez, M.; Boeré, R. T. *Acta Crystallogr. C* **1995**, *51*, 2118. (d) Haynes, D. A. *CrystEngComm* **2011**, *13*, 4793.

(28) (a) Vegas, A.; Pérez-Salazar, A.; Banister, A. J.; Hey, R. G. *J. Chem. Soc., Dalton Trans.* **1980**, 1812. (b) Banister, A. J.; Rawson, J. M. *Adv. Heterocycl. Chem.* **1995**, *62*, 137. (c) Awere, E. G.; Burford, N.; Haddon, R. C.; Parsons, S.; Passmore, J.; Waszczak, J. V.; White, P. S. *Inorg. Chem.* **1990**, *29*, 4821. (d) Awere, E. G.; Burford, N.; Mailer, C.; Passmore, J.; Schriver, M. J.; White, P. S.; Banister, A. J.; Oberhammer, M.; Sutcliffe, L. H. *J. Chem. Soc., Chem. Commun.* **1987**, 66. (e) Alberola, A.; Clements, O. P.; Collis, R. J.; Cubbitt, L.; Grant, C. M.; Less, R. J.; Oakley, R. T.; Rawson, J. M.; Reed, R. W.; Robertson, C. M. *Cryst. Growth Des.* **2008**, *8*, 155.

(29) (a) Bestari, K.; Cordes, A. W.; Oakley, R. T.; Young, K. M. *J. Am. Chem. Soc.* **1990**, *112*, 2249. (b) Feeder, N.; Less, R. J.; Rawson, J. M.; Oliete, P.; Palacio, F. *Chem. Commun.* **2000**, 2449.

(30) Beneberu, H. Z.; Tian, Y.-H.; Kertesz, M. *Phys. Chem. Chem. Phys.* **2012**, *14*, 10713.

(31) (a) Small, D.; Zaitsev, V.; Jung, Y.; Rosokha, S. V.; Head-Gordon, M.; Kochi, J. K. *J. Am. Chem. Soc.* **2004**, *126*, 13850. (b) Mota, F.; Miller, J. S.; Novoa, J. J. *J. Am. Chem. Soc.* **2009**, *131*, 7699. (c) Clarke, C. S.; Jornet-Somoza, J.; Mota, F.; Novoa, J. J.; Deumal, M. *J. Am. Chem. Soc.* **2010**, *132*, 17817.

(32) Barclay, T. M.; Beer, L.; Cordes, A. W.; Oakley, R. T.; Preuss, K. E.; Taylor, N. J.; Reed, R. W. *Chem. Commun.* **1999**, 531.

(33) (a) Cozzolino, A. F.; Vargas-Baca, I.; Mansour, S.; Mahmoudkhani, A. H. *J. Am. Chem. Soc.* **2005**, *127*, 3184. (b) Cozzolino, F.; Vargas-Baca, I. *Cryst. Growth Des.* **2011**, *11*, 668. (c) Risto, M.; Assoud, A.; Winter, S. M.; Oilunkaniemi, R.; Laitinen, R. S.; Oakley, R. T. *Inorg. Chem.* **2008**, *47*, 10100.

(34) (a) Cornil, J.; Beljonne, D.; Calbert, J.-P.; Brédas, J.-L. *Adv. Mater.* **2001**, *13*, 1053. (b) Koren, A. B.; Curtis, M. D.; Francis, A. H.; Kampf, J. W. *J. Am. Chem. Soc.* **2003**, *125*, 5040.

(35) We have not observed luminescence from either β-**1a** or β-**1b**.

(36) Based on these energy surfaces, the photogeneration of the dimer from the radicals, that is, the reverse LIRT process, appears unlikely, and indeed no such effect has been seen experimentally.

(37) (a) Jeftić, J.; Hauser, A. *J. Phys. Chem. B* **1997**, *101*, 10262. (b) Gütlich, P.; Ksenofontov, V.; Gaspar, A. B. *Coord. Chem. Rev.* **2005**, *249*, 1811.

(38) Létard, J.-F. *J. Mater. Chem.* **2006**, *16*, 2550.

(39) To our knowledge, the highest *T* observed for a LIESST state is 180 K. See: Li, D.; Clérac, R.; Roubeau, O.; Harté, E.; Mathoniére, C.; Le Bris, R.; Holmes, S. M. *J. Am. Chem. Soc.* **2008**, *130*, 252.

(40) *SAINT*, version 6.22; Bruker Advanced X-ray Solutions, Inc.: Madison, WI, 2001.

(41) Sheldrick, G. M. *Acta Crystallogr. A* **1990**, *46*, 467.

(42) Sheldrick, G. M. *SHELXL-97, Program for the Refinement of Crystal Structures*; University of Gottingen: Gottingen, Germany, 1997.

(43) *SHELXTL, Program Library for Structure Solution and Molecular Graphics*, version 6.12; Bruker Advanced X-ray Solutions, Inc.: Madison, WI, 2001.

(44) Smith, J. S.; Desgreniers, S. *J. Synchrotron Radiat.* **2009**, *16*, 83.

(45) Boultif, A.; Louer, D. *J. Appl. Crystallogr.* **2004**, *37*, 724.

(46) David, W. I. F.; Shankland, K.; van de Streek, J.; Pidcock, E.; Motherwell, W. D. S.; Cole, J. C. *J. Appl. Crystallogr.* **2006**, *39*, 910.

(47) Rietveld, H. M. *J. Appl. Crystallogr.* **1969**, *2*, 65.

(48) Larson, A. C.; Von Dreele, R. B. *General Structure Analysis System (GSAS); Report LAUR* Los Alamos National Laboratory : Los Alamos, NM, 2000; pp 86−748.

(49) Secco, R. A. *Can. J. Phys.* **1995**, *73*, 287.

(50) Secco, R. A.; Schloessin, H. H. *J. Appl. Phys.* **1986**, *60*, 1625.

(51) Carlin, R. L. *Magnetochemistry*; Springer-Verlag, New York, 1986.

(52) Frisch, M. J.; Trucks, G. W.; Schlegel, H. B.; Scuseria, G. E.; Robb, M. A.; Cheeseman, J. R.; Scalmani, G.; Barone, V.; Mennucci, B.; Petersson, G. A.; Nakatsuji, H.; Caricato, M.; Li, X.; Hratchian, H. P.; Izmaylov, A. F.; Bloino, J.; Zheng, G.; Sonnenberg, J. L.; Hada, M.; Ehara, M.; Toyota, K.; Fukuda, R.; Hasegawa, J.; Ishida, M.; Nakajima, T.; Honda, Y.; Kitao, O.; Nakai, H.; Vreven, T.; Montgomery, J. A., Jr.; Peralta, J. E.; Ogliaro, F.; Bearpark, M.; Heyd, J. J.; Brothers, E.; Kudin, K. N.; Staroverov, V. N.; Kobayashi, R.; Normand, J.; Raghavachari, K.; Rendell, A.; Burant, J. C. Iyengar, S. S.; Tomasi, J.; Cossi, M.; Rega, N.; Millam, N. J.; Klene, M.; Knox, J. E.; Cross, J. B.; Bakken, V.; Adamo, C.; Jaramillo, J.; Gomperts, R.; Stratmann, R. E.; Yazyev, O.; Austin, A. J.; Cammi, R.; Pomelli, C.; Ochterski, J. W.; Martin, R. W.; Morokuma, K.; Zakrzewski, V. G.; Voth, G. A.; Salvador, P.; Dannenberg, J. J.; Dapprich, S.; Daniels, A. D.; Farkas, O.; Foresman, J. B.; Ortiz, J. V.; Cioslowski, J.; Fox, D. J. *Gaussian 09*, revision A.02; Gaussian, Inc.: Wallingford, CT, 2009.

(53) Neese, F. *Wiley Interdiscip. Rev. Comput. Mol. Sci.* **2012**, *2*, 73.